Pacific Northwest
NATIONAL LABORATORY

PNNL-37476

# Radiation Imaging with Event Camera

March 2025

Kevin Bertschinger
Benjamin McDonald

U.S. DEPARTMENT OF ENERGY

Prepared for the U.S. Department of Energy
under Contract DE-AC05-76RL01830

PACIFIC NORTHWEST NATIONAL LABORATORY
*operated by*
BATTELLE
*for the*
UNITED STATES DEPARTMENT OF ENERGY
*under Contract DE-AC05-76RL01830*

**Printed in the United States of America**

**Available to DOE and DOE contractors from**
**the Office of Scientific and Technical Information,**
**P.O. Box 62, Oak Ridge, TN 37831-0062**
**www.osti.gov**
**ph: (865) 576-8401**
**fox: (865) 576-5728**
**email: reports@osti.gov**

**Available to the public from the National Technical Information Service**
**5301 Shawnee Rd., Alexandria, VA 22312**
**ph: (800) 553-NTIS (6847)**
**or (703) 605-6000**
**email: info@ntis.gov**
**Online ordering: http://www.ntis.gov**

PNNL-37476

# Radiation Imaging with Event Camera

March 2025

Kevin Bertschinger
Benjamin McDonald

Prepared for
the U.S. Department of Energy
under Contract DE-AC05-76RL01830

Pacific Northwest National Laboratory
Richland, Washington 99354

## Abstract

Neuromorphic or event-based imaging is a new, commercially available sensor technology inspired by how the human eye works. Instead of measuring frames at a fixed rate, the camera measures changes in pixel intensity asynchronously. This difference in readout architecture results in a high dynamic range and low latency. Event-based cameras have been used in a variety of applications, including object tracking, navigation, and lidar technologies. However, event-based cameras have not been adequately researched for their ability to image high-energy particles. This report explores the use of an event camera for imaging alpha, beta, and X-rays particles, when coupled with scintillator screens to convert high-energy particles into visible light. Methods to process event data were developed and are presented here, along with the results. The event camera can measure alpha and beta particles with comparable performance to that of a conventional camera. Event cameras can also image higher-activity sources and offer the possibility of discriminating particle interaction types on the basis of timing differences, which typical cameras cannot do. Additionally, event cameras can image objects with an X-ray source when the source strength dynamically changes but does not create a high-contrast image during static X-ray measurement.

# Summary

Inspired by how the human eye works, neuromorphic or event-based imaging cameras have been developed and are commercially available. Instead of capturing image frames, event cameras read out changes in pixel intensity asynchronously. Event cameras have been utilized in a variety of applications, from robotic systems to object tracking and lidar technologies. Event cameras have been insufficiently investigated for their ability to detect and image high-energy particles. This report details the evaluation of an event camera's capability to measure alpha rays, beta rays, and X-rays and the comparison of its performance with that of traditional complementary metal oxide semiconductor cameras.

For the processing of event data, two different representations were explored. The first converts events to direct counts per pixel. This is analogous to seeing an intensity image and is useful for visualizing the captured data and comparing it to conventional images. In addition, clustering algorithms can be applied to event data to count scintillation flashes. In the second type of image representation, the time stamp of a captured event is mapped into a pixel value, creating an image that shows where events have occurred in time. This type of representation is unique to an event camera and can show when and where scintillation flashes occur within a frame. Connected-component algorithms can be applied to the time stamp representation to understand the evolution of scintillation interactions.

Measurements of alpha and beta sources were obtained with both a conventional camera optimized for radiation imaging and an event camera for comparison. The comparison revealed that the same qualitative features were present in both the event count images and conventional images. For alpha measurements, the event camera had a lower count rate than the conventional imaging system, which is likely due to the scintillation flashes appearing more sparsely on the event camera images than on the images from the conventional imaging system. Subsequently, for beta measurements, the event camera showed a higher count rate. This is likely due to noise contributing to the overall count due to the smaller cluster size. Furthermore, the event camera exhibited capabilities not demonstrated by the conventional imaging system in that it could measure higher-activity sources and observe some differences in scintillator decay times.

For the measurement of a static X-ray source, only event count images were investigated. During the static X-ray measurement, the event camera did show signs of elevated event count rates. Overall, the image contrast was poor, and only a few features were discernible. However, when the X-ray tube ramped up in energy or turned off, a very clear image formed for a few seconds. It is possible that during these transitions, the X-ray flux is momentarily low enough to not overwhelm the event-based camera. When the X-ray source is fully powered on, the flux may be too high for the camera to process all of the scintillation events. More investigation is needed across a stepped range of X-ray currents and end point energies.

## Acronyms and Abbreviations

EV - event vision

iQID - ionizing-radiation quantum imaging detector

# Contents

Abstract ..... ii
Summary ..... iii
Acronyms and Abbreviations ..... iv
1.0 Introduction ..... 1
2.0 Materials and Methods ..... 2
3.0 Data Processing ..... 5
3.1 iQIDs Processing ..... 5
3.2 Event Count Image ..... 5
3.3 Temporal Image ..... 6
3.4 Clustering of Different Data Formats ..... 6
4.0 Results and Discussion ..... 7
4.1 Count Rate Images and Ground Truth Comparison ..... 7
4.1.1 Alpha Source Measurements ..... 7
4.1.2 Beta Measurement ..... 8
4.1.3 Dual Alpha and Beta Measurement ..... 9
4.1.4 Mylar Sheet Experiment ..... 10
4.1.5 X-Ray Event Count Images ..... 13
4.2 Temporal Images ..... 15
Conclusion and Path Forward ..... 18
5.0 References ..... 19

# Figures

Figure 1: Ionizing-radiation quantum imaging detector. A.) Side view showing image intensifier and enclosure containing the adjustable lens and camera. B.) Top view showing the scintillator screen, alpha source on glass microcapillary arrays (black), and beta source. ..... 3
Figure 2: Quantum efficiency of FLIR Grasshopper 3 GS3-U3-51S5M-C camera. ..... 3
Figure 3: Spectral sensitivity of the EVS (from https://www.framos.com/wp-content/uploads/FSM-IMX636-Devkit-Datasheet.pdf). ..... 4
Figure 4: Emission spectrum for the Ej-444 scintillator screen. ..... 4
Figure 6: A.) Image of Po-210 alpha particles made with the iQID CMOS camera. B.) Image of Po-210 event counts produced by the iQID with the EV camera. ..... 8
Figure 7: A.) Sr-90 0.01 $\mu Ci$ measured using a CMOS camera with intensity values. B.) Beta measurement using an EV camera with *on* event counts. Both cameras can image the beta source with the same qualitative features. ..... 9

Figure 8: Po-210 alpha source 250 $\mu Ci$ measured on glass capillary arrays, with 1 mm thick glass (middle top of image) and Sr-90 $0.01$ $\mu Ci$ beta source (middle bottom of image). ....10

Figure 9: Po-210 500 $\mu Ci$ source measured with different mylar sheets attenuating the overall counts. A.) Raw Po-210 source with no attenuation. B.) Po-210 source with one mylar sheet of attenuation. C.) Po-210 source with two mylar sheets of attenuation. D.) Po-210 source with three mylar sheets of attenuation. E.) Po-210 source with four mylar sheets of attenuation. The diagonal lines are likely caused by folds in some of the stacked mylar sheets, which caused high attenuation at the highest thicknesses. ....11

Figure 10: Count rate attenuation of mylar film as thickness increases. ....12

Figure 11: A.) bare Po-210 $500$ $\mu Ci$ source. B.) Po-210 alpha source attenuated by one mylar sheet. In both cases, clusters are discernible even at a high-count rate because of the low latency of the EV camera. The images are captured with a time window of 1000 $\mu s$ or 1000 FPS. ....13

Figure 12: X-ray image when the X-ray tube ramped up. During the ramp up, the EV camera saw an influx of on events, and an image of the object was observable. ....13

Figure 13: X-ray image when the X-ray tube turned off. During the off procedure, the EV camera saw an influx of off events, and an image of the object was observable. C.) The temporal profile of events per pixel along the x-coordinate. The profile shows an *on* event, and a stream of *off* events corresponding to the decay of gadox. ....14

Figure 14: X-ray image of an object captured with the CMOS camera. The CMOS camera was able to capture the contrast difference of the object through most of the X-ray measurement. ....15

Figure 15: Time stamp of an event can be mapped to the pixel location to obtain a heat map showing the time when the event occurred. A.) Heat map of the time of on events for the scintillations. B.) Heat map of the time of off events for the scintillation. ....16

Figure 16: (Right): Imaging a Po-210 250 $\mu Ci$ source and replacing the pixel value with the time stamp of an event over a large time interval. The places where a large scintillation occurs are easily apparent. (Left): For this case, the image intensifier gain was increased. The z-axis is in units of showing when the events occurred with units of microseonds. ....16

# Tables

Table 1: Specifications of the different cameras used in this study. ....3

Table 2: Relative response for SilkeyEVcam at different wavelengths. ....4

# 1.0 Introduction

Humans can visualize and process complex visual information with greater accuracy and efficiency than conventional computers and camera systems. Inspired by the efficiencies of biological systems, hardware has been developed to mimic similar processes of biological systems. A new technology considered in this report is neuromorphic or event-based imaging [1]. Event vision (EV) cameras provide new capabilities not seen in conventional cameras that will be beneficial to nuclear radiation imaging applications.

Instead of measuring frames, events cameras measure changes in pixel intensity asynchronously. This results in sparse data representation since only changes in a scene are measured rather than the entire scene being imaged at a fixed frame rate. In addition, the alternative readout architecture promotes low latency, resulting in faster imaging. This means the event camera can perform high-speed imaging while reducing redundant information. In addition, event cameras measure changes in light intensity across a logarithmic scale. This results in a high dynamic range of 120 dB, allowing the event camera to capture greater contrast between in very dark scenes and very bright scenes. To achieve similar results with a conventional camera, the exposure time and frame rates need to be adjusted over multiple acquisitions. Finally, the more efficient readout results in a low power consumption for such a high-speed imaging system [1].

Event cameras have been tested for a variety of applications, such as high-speed imaging and robotic systems as well as navigation, lidar, and object tracking technologies [2-5]. For radiation applications, event cameras have been used to image a moving object using X-rays and by tracking an X-ray beam [6, 7]. While research has explored the other applications of EV cameras, much less research has been dedicated to investigating the capabilities of EV cameras for imaging with ionizing radiation.

This report describes a preliminary investigation of the utility of using event-based imaging to detect high-energy particles, such as alpha, beta, and X-ray particles, with a scintillator screen. One goal was to evaluate the performance of EV cameras in areas where conventional cameras tend to struggle. For example, because of its low latency, an EV camera should be able to measure sources at higher activity levels than a conventional camera, which is limited by its lower frame rate. Accordingly, an EV camera should be able to measure alpha and beta particles simultaneously because of its high dynamic range.

# 2.0 Materials and Methods

To characterize an EV camera's capability to measure high-energy particles, a series of experiments were conducted to measure different particle types: alpha, beta, and X-ray. Scintillator screens were used to convert particle interactions to visible light. In addition, measurements were made with a conventional camera in the same configurations so that its performance could be compared with that of the EV camera.

For the measurement of alpha and beta particles, the experimental setup was nearly identical to a setup previously used for measurement with an ionizing-radiation quantum imaging detector (iQID) [8]. The only difference between the two configurations was that the complementary metal oxide semiconductor (CMOS) camera (FLIR Grasshopper3) was switched with the EV camera. The system consisted of a scintillator screen made from two different materials for alpha and beta detection. The first layer was ZnS:Ag for alpha emission, and the second layer was EJ-212 for beta detection (EJ-444, Eljen technology). The scintillator was in contact with a 10 cm × 10 cm fiber optic taper (Incom, Inc), which was in turn coupled to a ø4 cm image intensifier (Proxivision). The intensified light was focused onto the camera using a standard adjustable lens. Po-210 alpha sources (NRD LLC) with $250\ \mu Ci$ and $500\ \mu Ci$ activity were measured with and without glass capillary arrays, which limit the alpha flux. A Sr-90 source (Isotope Products) with an activity of 0.01 $\mu Ci$ was used for the beta measurements.

For the X-ray measurements, an X-ray tube was used to generate a bremsstrahlung source producing X-rays of energy levels up to 160 keV (XRG, Comet X-ray). The X-ray source was placed behind an object to image, which attenuated the X-rays as they traveled to a scintillator screen (gadolinium oxysulfide, Mitsubishi Chemical Corp. DRZ series). Scintillations were reflected off a mirror and captured by a CMOS camera. The CMOS camera (Basler ace) was placed next to the EV camera to capture images with both sensors simultaneously.

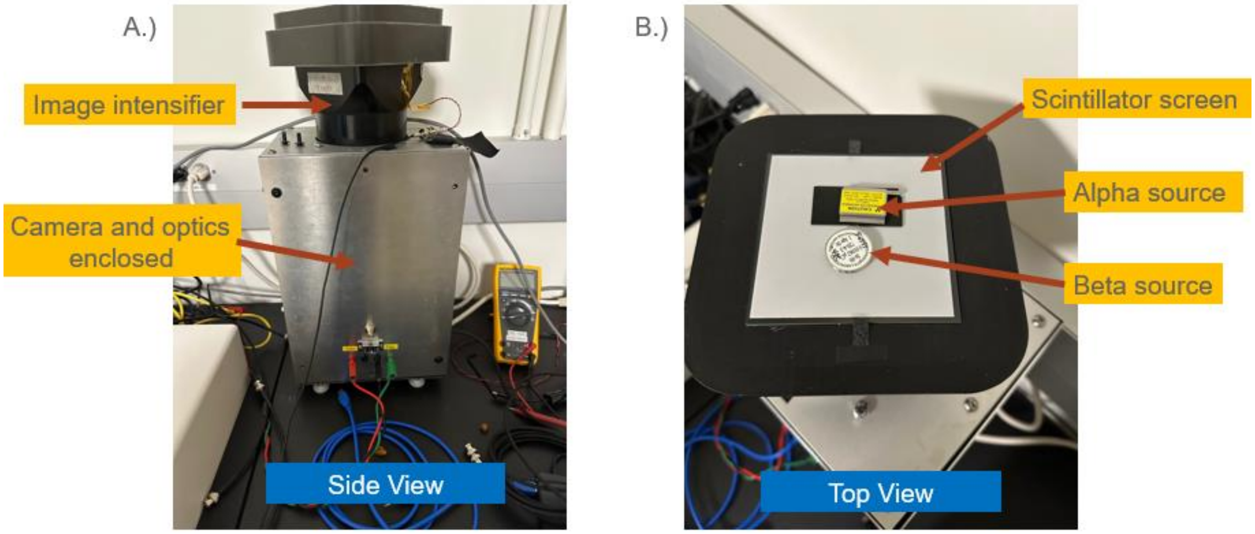


Figure 1: Ionizing-radiation quantum imaging detector. A.) Side view showing image intensifier and enclosure containing the adjustable lens and camera. B.) Top view showing the scintillator screen, alpha source on glass microcapillary arrays (black), and beta source.

Table 1: Specifications of the different cameras used in this study.

| Camera Model | Pixel Pitch ($\mu m$) | Latency | Sensor Size | Power | Dynamic Range |
|---|---|---|---|---|---|
| SilkEvCam HD, Sony IMX636 | 4.86 x 4.86 | 100 $\mu s$ (10K fps) | 1280 x 720 (3/4") | 80 mW | >120 dB |
| FLIR Grasshopper 3 GS3-U3-51S5M-C | 3.45 x 3.45 | 75 max fps | 2448 x 2048 (2/3") | 4.5 W | 40.09 dB |
| Basler ace | 6.9 × 6.9 | 291 fps | 720 x 540 | 3.2 W | 57.2 dB |

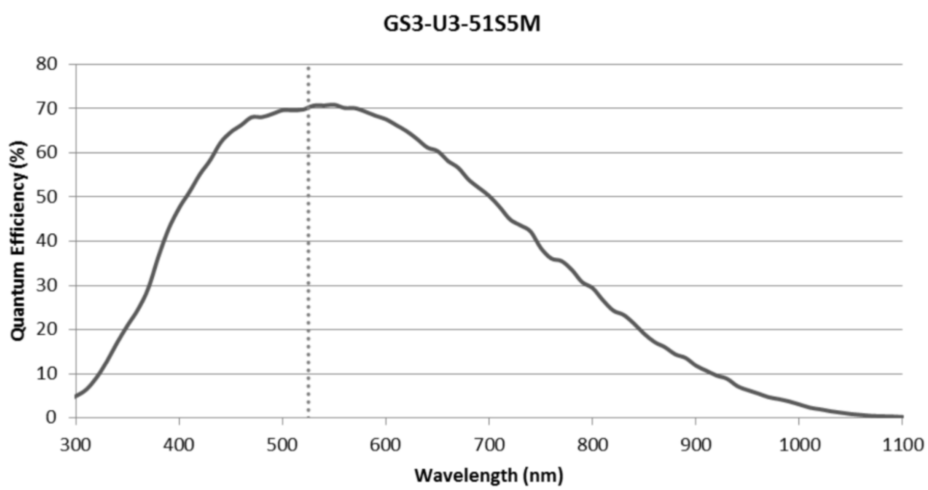


Figure 2: Quantum efficiency of FLIR Grasshopper 3 GS3-U3-51S5M-C camera.

Materials and Methods

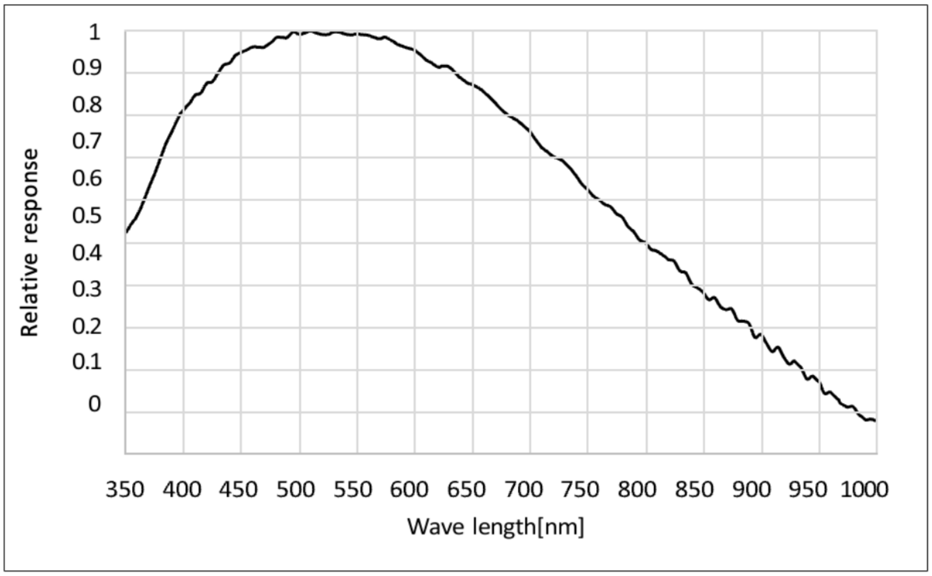


Figure 3: Spectral sensitivity of the EVS (from https://www.framos.com/wp-content/uploads/FSM-IMX636-Devkit-Datasheet.pdf).

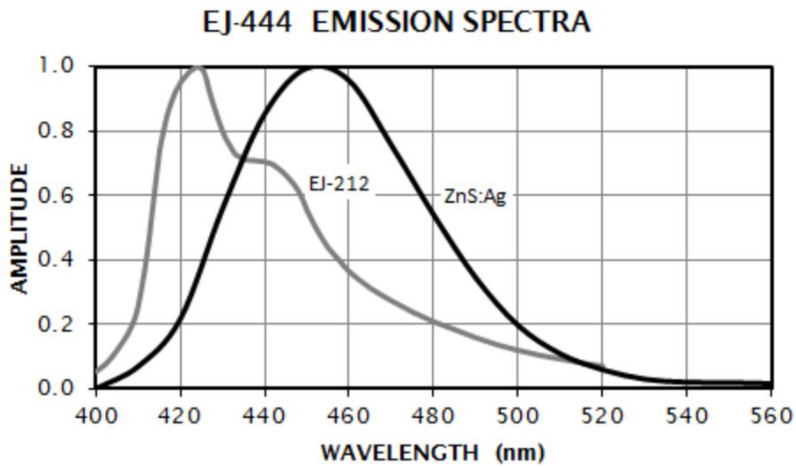


Figure 4: Emission spectrum for the Ej-444 scintillator screen.

Table 2: Relative response for SilkeyEVcam at different wavelengths.

| LED Wavelength | 455nm | 505nm | 625nm | 850nm | 940nm |
|---|---|---|---|---|---|
| IMX636/IMX646 | 88% | 100% | 92% | 39% | 18% |

# 3.0 Data Processing

The data was processed to separate noise from scintillation events. There are two systems used to measure radioactive sources in this report with slightly different processing methods. The first was the iQID system used to quantify and ground truth the count rate of measured sources. The second was the EV camera using a similar set up as the iQID.

Instead of producing frame data the event camera produces a list of events. An event data consist of a pair of (x,y) coordinates for the pixel location of where the event occurred, a time stamp (t) for when the event occurred, and a polarity change for *on* event (1, increase in brightness) and an *off* event (0, decrease in brightness). This corresponds to a list of values in the format (x, y, t, P). For this reason, the list of events was processed a specific way to form an image. In addition, clusters can be found in the image, and scintillation events can be counted. Since the event camera has a low latency, high activity sources produce a high number of events, and loading all the data at once can be troublesome for a computer system. For this reason, chunks of data are iterated through, and frames are created to produce the desired results over a series of time intervals.

Since the EV camera does not produce standard intensity images like a conventional camera, the event data will be represented as an image in two different formats. The first representation will capture total events over a time interval into a frame and will be called an *event count image* or representation. The second representation will convert the time stamp of the event to pixel location, and this depiction will be called a *temporal image* or *time stamp image*.

## 3.1 iQIDs Processing

The following section outlines the processing steps used by the iQID system. The iQID system is used to process data and ground truth data collected with the event camera.

1. Framerate and exposure are set for particle (alpha or beta) being measured.

2. Raw frames are analyzed to determine intensity and cluster size thresholds

3. A median filter is applied.

4. A connected components algorithm is applied to captured scintillation clusters above set thresholds (area and intensity).

5. Clusters or cluster centroids are computed and histogrammed in a 2-D array to create a final image.

## 3.2 Event Count Image

An image of total accumulated events is constructed for *on* or *off* events. The following steps outline the procedure.

1. Pull chunk of events for a given time interval. The event data is a list of elements grouped together by position (x,y), time of the event (t), and polarity for *on* (1) or *off* (0). The full format is (x,y,t,P).

2. Events are filtered into *on* and *off* events by polarity.

3. Each polarity is summed for pixel (x,y) for each time interval corresponding to an event.

4. Each count total pair of then mapped to the corresponding pixel position to create an image of counts.

5. The image count is stored in a 2-D array.

6. A median filter is applied to remove noise pixel that do not form a cluster of events.

7. Steps 1 through 5 are repeated and added to the previous 2-D array to create a total count of events image.

Note for X-ray measurements, the median filter is not applied, and images are not summed. Only steps 1-4 are used to create an image.

## 3.3 Temporal Image

In conjunction with investigating event counts, a unique component to the event camera is high temporal resolution and asynchronous readout. This enables the ability to assign the time of the events to the pixel value. This way scintillation events can be see when and where they occurred when reconstructing frames from event data. The following procedure outlines the procedure for constructing temporal images.

1. Pull chuck of event data for a given time interval. The event data is a list of elements grouped together by position (x,y), time of the event (t), and polarity for on (1) or off (0). The full format is (x,y,t,P).

2. Events are filtered into an array of *on* or *off* events based on polarity.

3. The time of the event is mapped to a 2-D array at the position (x,y).

4. The 2-D array is normalized with respect to the maximum value in the 2-D array.

5. The 2-D array is then converted to a uint8 format.

6. A median filter is then applied.

7. Connected-component analysis is applied to find clumps of pixels in the 2-D array.

## 3.4 Clustering of Different Data Formats

The iQiD used a connected components algorithm to identify a cluster or blob of illuminated pixels that are connected. The cluster of pixels is identified as a scintillation flash. A statistical analysis is then performed on the results of the connected components and is then used to optimize the median filter to remove noise and only identify correct scintillation flashes. The optimized clusters are then used to count total scintillation flashes (typically one per incident particle) over a given time span. Connected-component analysis is a standard image processing technique and can be found in most image processing libraries. For this analysis, the OpenCV library was used within Python.

# 4.0 Results and Discussion

The following section outlines the measurements made for alpha, beta, and X-ray sources. The two different representations of the event data are analyzed and presented in two separate sections. Since the event count images showed similar features to the intensity images, a direct comparison is made between intensity images and event count images. For the section on temporal images, only the clustering ability is compared to measurements made by the iQID.

## 4.1 Count Rate Images and Ground Truth Comparison

### 4.1.1 Alpha Source Measurements

An alpha source of Po-210 with 250 $\mu Ci$ activity was used for alpha source measurements. The average energy of the emitted alphas is around 3 MeV based on alpha spectrometry measurements. The source produced too many events to detect with a conventional camera, and to reduce off-angle emission, the source was placed on top of two, side-by-side 25 x 25 x 1 $mm^3$ glass microcapillary arrays. The hole size of the array was 25 μm with 4.6 μm septal thickness. The small gap between the glass plates provided a narrow path for alpha particles to travel from the source to the scintillator. This is seen as a bright line in Figure 5. The three rectangular areas are alpha counts through the capillary array, with gaps from a protective grid. The iQID lens assembly was focused for the CMOS camera and left in the same configuration for the EV camera to draw a fair comparison. For this reason, the data collected with the EV camera was slightly out of focus. Data was also collected with the lens in focus for the EV camera, which showed better spatial resolution.

Analysis showed that *on* events showed more consistency than *off* events. This is possibly because of the fast decay time of the ZnS:Ag scintillator (~200 ns), which is shorter than the typical timing latency of the EV camera (100 μs). For this reason, only *on* events were summed during the image reconstruction. The positive counts of the EV camera showed comparable features to those of the CMOS camera. With both cameras, a high count was observed at the edge between the two capillary plates. The spacing between the microcapillary arrays with lower counts was present in those regions.

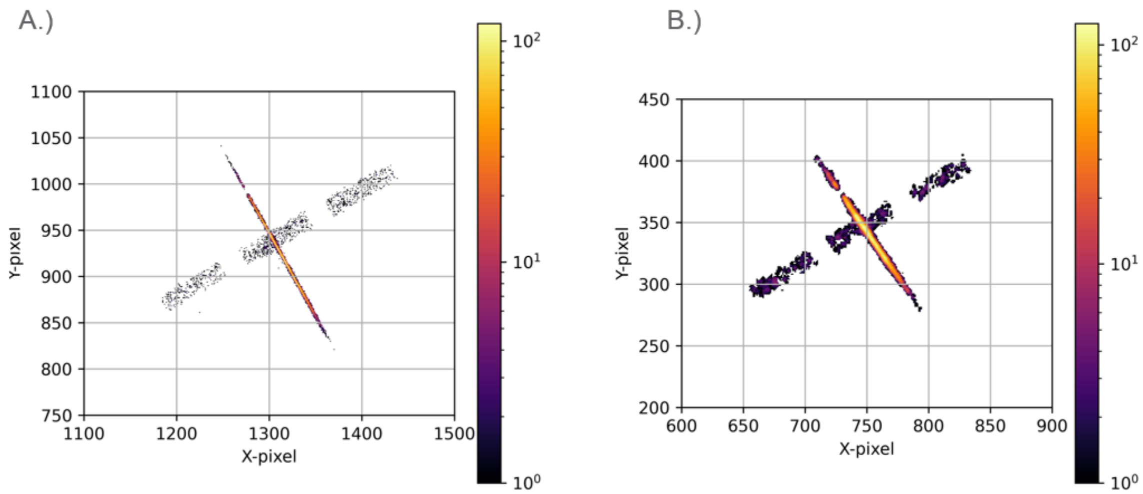


Figure 5: A.) Image of Po-210 alpha particles made with the iQID CMOS camera. B.) Image of Po-210 event counts produced by the iQID with the EV camera.

When connected-component analysis was performed to identify clusters during the measurements, the iQiD system found $62.5 \pm 3.165$ counts per second (CPS), whereas the EV camera showed $14 \pm 1.32$ CPS. The discrepancy between these cluster rates likely has a few causes. First, the iQID system was fully optimized for measuring the alpha source. Second, the scintillation flashes appeared to be sparse instead of fully connected for the EV camera. This was most apparent when the events were represented as a temporal image (Figure 10), as described in section 4.2. The EV and CMOS sensors have similar quantum efficiencies, so the differing count rates between the cameras likely have to do with the varying pixel sizes, optical focus, and cluster thresholds used in the analysis. The EV camera has larger pixels than the CMOS and was in poorer focus. Further, we later learned that the clusters on the CMOS camera was so large in some cases that they were being divided into multiple clusters, overpredicting the true alpha counting rate.

### 4.1.2 Beta Measurement

In addition to alpha sources, the system can also measure beta sources. The beta sources were less energetic and produced dimmer scintillation flashes. To compare a conventional CMOS to the EV camera, a Sr-90 source with 0.01 $\mu Ci$ was measured. Under the same conditions, the EV camera captured much fewer beta emissions than the CMOS camera did. For this reason, the image intensifier gain was increased to 1.4 V for the EV camera, whereas 1.0 V was used for the CMOS camera.

The CMOS and EV camera both showed similar features when capturing the circular outline of the button source and the varying intensity pattern inside the button. The EV camera exhibited a greater spatial resolution than the CMOS camera when capturing finer clusters. The count rate was found to be 55.60 $\pm 2.92$ CPS for the CMOS camera and $72.44 \pm 3.65$ CPS for the EV camera. The higher CPS likely contributed to the beta source having a smaller cluster size in the EV camera results than in the CMOS results. In addition, the increase in the image intensifier gain likely contributed to more noise being present in the measurement. The beta counting rates were closer in magnitude than the alpha rates, which may be due to the iQID scintillation flashes from the beta interactions being smaller, and less likely to be counted as multiple events.

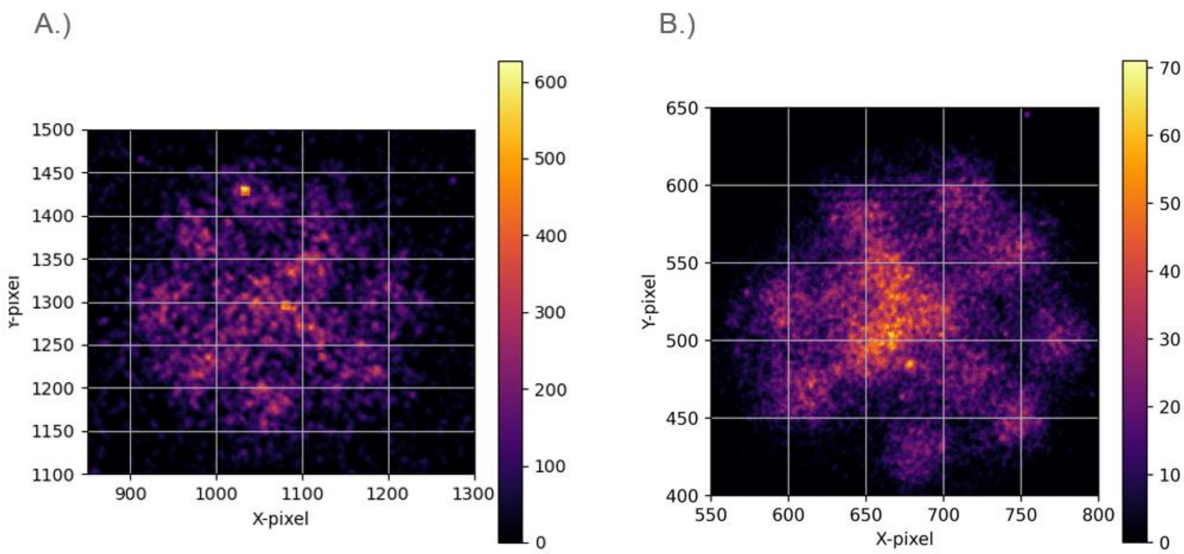


Figure 6: A.) Sr-90 0.01 $\mu Ci$ measured using a CMOS camera with intensity values. B.) Beta measurement using an EV camera with *on* event counts. Both cameras can image the beta source with the same qualitative features.

### 4.1.3 Dual Alpha and Beta Measurement

Event cameras measure changes in intensity on a logarithmic scale. This results in a high dynamic range (>120 dB). A CMOS camera, with a dynamic range of 67 dB, cannot easily image beta and alpha sources simultaneously since the difference in light brightness is large and requires setting a high gain on the image intensifier to detect betas, which then saturate alpha events. The EV camera should be able to measure alpha and beta sources simultaneously due to the high dynamic range. For this reason, the alpha and beta sources were combined for one measurement. The alpha Po-210 source was placed on a single glass capillary arrays following the process described in section 4.1.1. Here there were some alpha events streaming past the edge of the array, visible as comet-shaped elevated regions in Figure 7. The beta source was the same Sr-90 used in section 4.1.2, with 0.01 $\mu Ci$ activity. The image intensifier was set to 1.4 V. The event data was converted to event count images and summed for 5 minutes, showing clear counts for the beta and alpha source. Comparable measurements with the iQID were not taken.

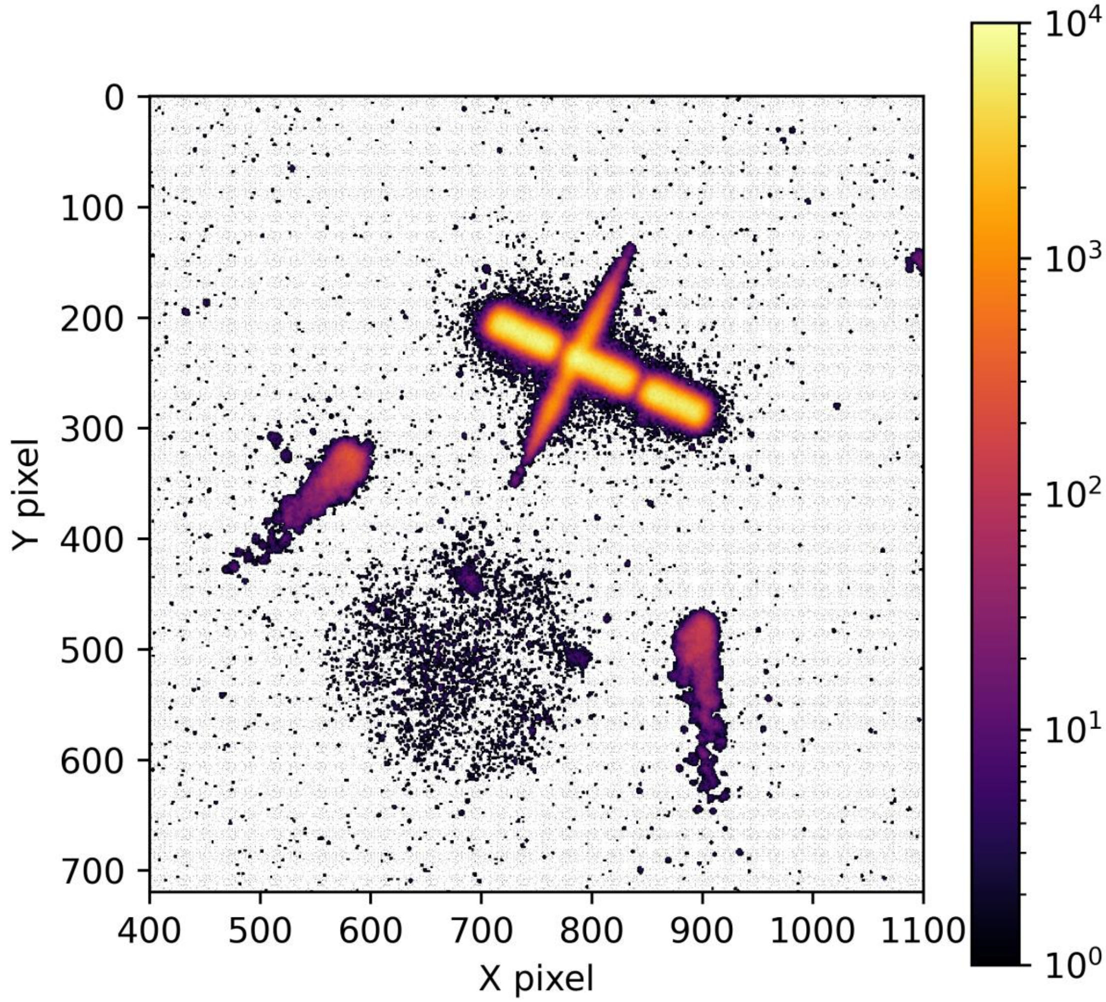


Figure 7: Po-210 alpha source 250 $\mu Ci$ measured on glass capillary arrays, with 1 mm thick glass (middle top of image) and Sr-90 $0.01$ $\mu Ci$ beta source (middle bottom of image).

### 4.1.4 Mylar Sheet Experiment

The event camera had a latency of approximately $100\ \mu s$. Though an event camera does not capture frames, translating the low latency to a frame rate that would result in imaging an object at a rate of 10,000 fps. For this reason, the event camera should be able to measure higher-activity sources than a CMOS camera can. To test high-activity count rate capability, a Po-210 alpha source with activity 500 $\mu Ci$ was placed directly on a ZnS:Ag scintillator sheet (25 μm ZnS:Ag with 25 μm plastic backing). Mylar sheets with 3.7 µm thickness were added between the scintillator and source to increasingly attenuate the alpha particles and reduce counting rates. The counts gradually decreased until five sheets of mylar were placed between the source and scintillator screen. The event count images can be seen in Figure 8. The source was not placed in the exact same position for each measurement.

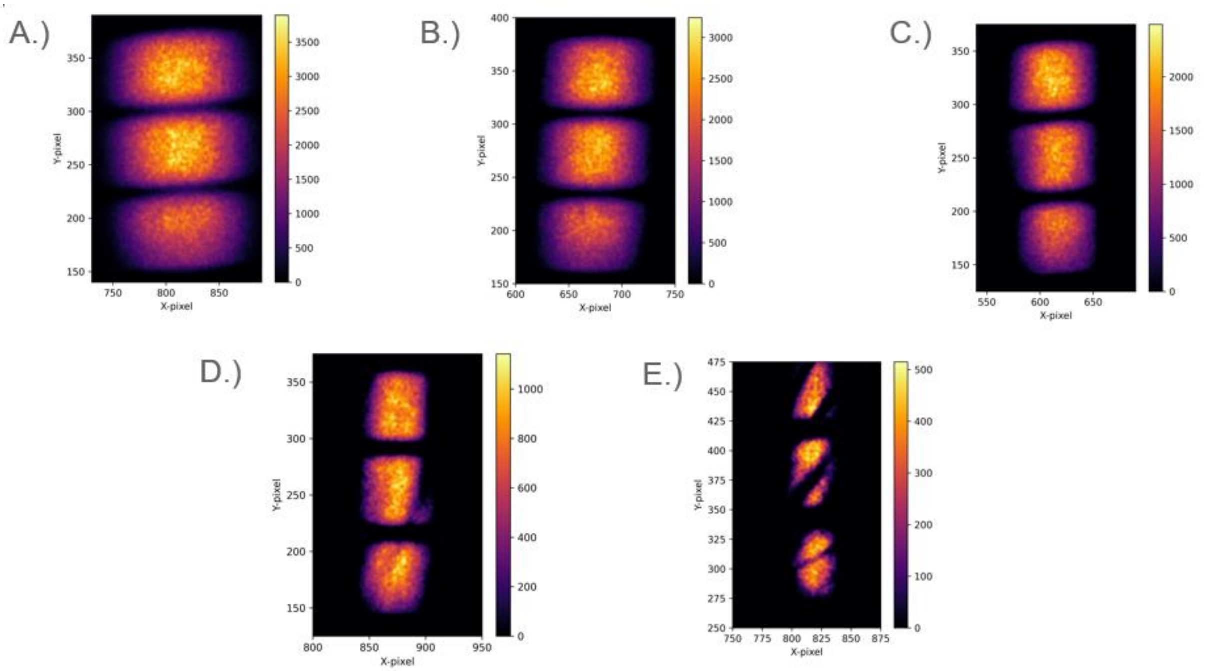


Figure 8: Po-210 500 $\mu Ci$ source measured with different mylar sheets attenuating the overall counts. A.) Raw Po-210 source with no attenuation. B.) Po-210 source with one mylar sheet of attenuation. C.) Po-210 source with two mylar sheets of attenuation. D.) Po-210 source with three mylar sheets of attenuation. E.) Po-210 source with four mylar sheets of attenuation. The diagonal lines are likely caused by folds in some of the stacked mylar sheets, which caused high attenuation at the highest thicknesses.

As the alpha emission was attenuated, the overall counts decreased, and the spatial extents of the source also decreased. At very high counting rates, spatial overlap of scintillation flashes can lead to larger clusters, which effectively cause a blurring effect in the processed images. Figure 5 shows images for a collimated similar source, where the dimensions were approximately 25 x 75 pixels for each of the three source rectangles (regions where alphas directly shine to the scintillator). Subsequently, the overall trend showed an exponentially decaying count as mylar sheets were added (Figure 9). The CMOS camera was unable to measure a source with such a high activity. The estimated alpha flux incident on the scintillator with no mylar is 4e6 alphas/s, an order of magnitude higher than the measured rate. This is likely a combination of the scintillator efficiency, undercounting from spatial pileup (overlapping events being counted as one), and other factors in the data acquisition and processing. The incident flux does not include any attenuation by the thin metal layers encapsulating the Po-210 material, which also may reduce the alpha flux significantly.

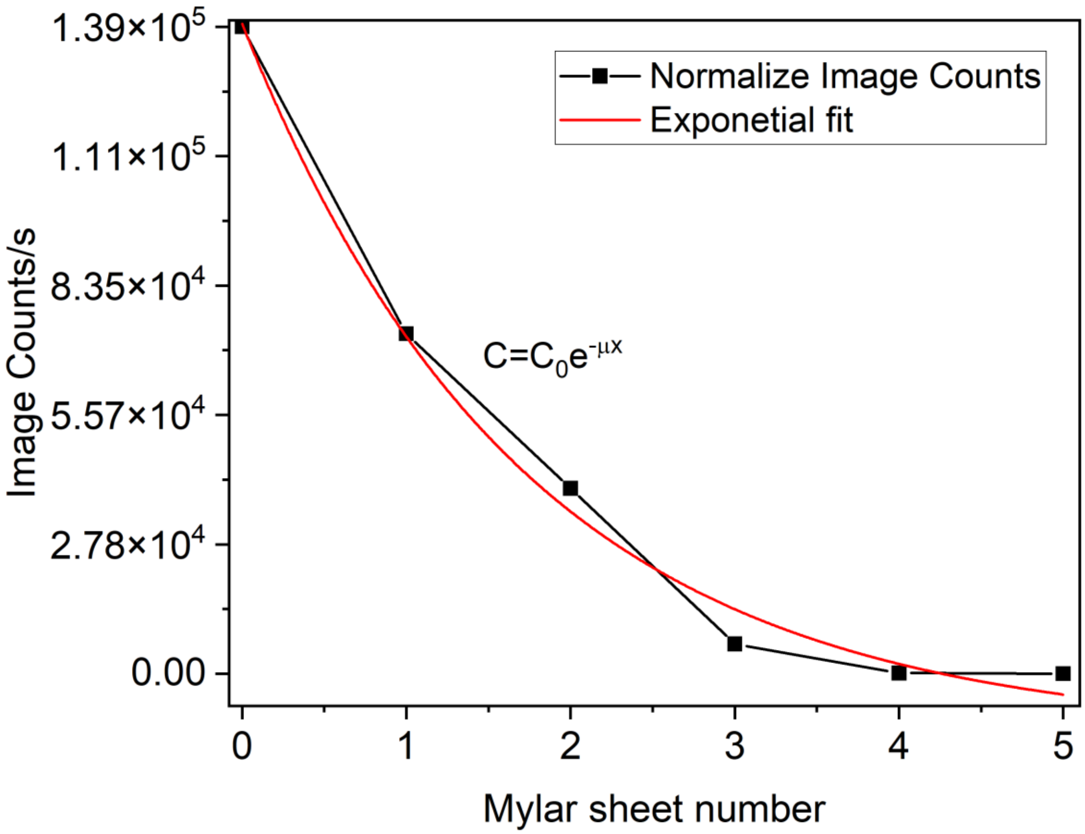


Figure 9: Count rate attenuation of mylar film as thickness increases.

Likewise, the mylar test showed that the EV camera did not saturate when exposed to a high activity source of $500\ \mu Ci$. In addition, adjusting the time interval allowed clusters to be seen and counted (Figure 10). There was likely some spatial overlap between scintillation flashes, but further investigation is needed to quantify how much. However, in the high-activity case, the EV camera was much more capable for measuring high-activity sources than a conventional CMOS camera.

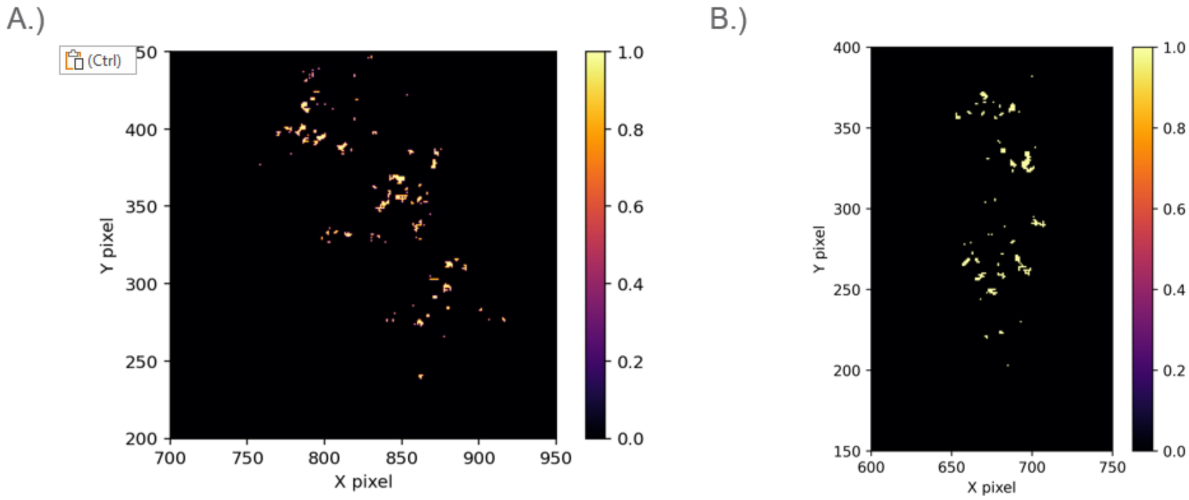


Figure 10: A.) bare Po-210 $500\ \mu Ci$ source. B.) Po-210 alpha source attenuated by one mylar sheet. In both cases, clusters are discernible even at a high-count rate because of the low latency of the EV camera. The images are captured with a time window of 1000 $\mu s$ or 1000 FPS.

### 4.1.5 X-Ray Event Count Images

A 10-minute X-ray measurement was captured as the X-ray tube ramped up in intensity. During the measurement, a clear image was discernible on two occasions for a few seconds. The first was when the X-ray tube ramped up, showing an influx of positive or *on* events (Figure 11). The second one was when the X-ray tube shut off, showing an influx of *off* events (Figure 12). A reference of the object captured with a CMOS camera is shown in Figure 13.

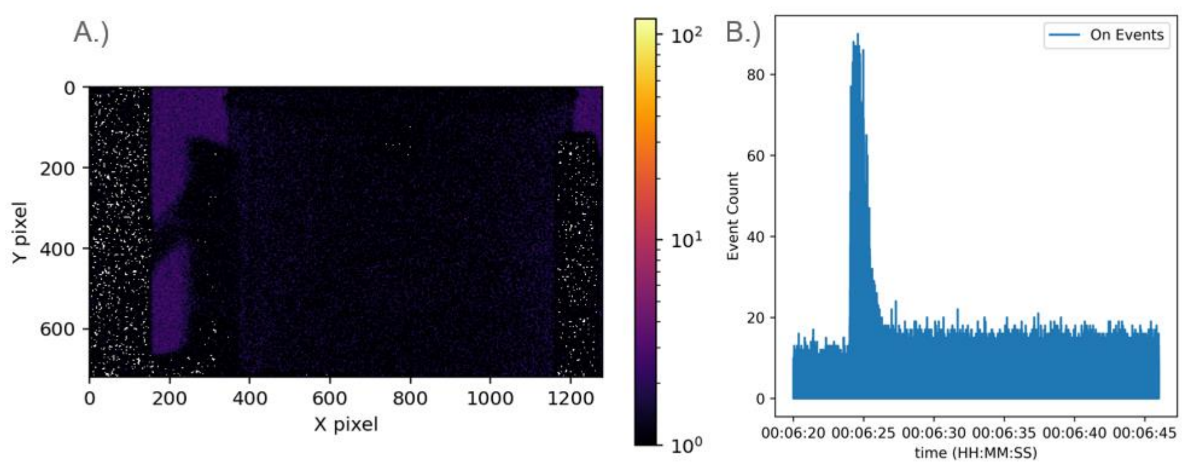


Figure 11: X-ray image when the X-ray tube ramped up. During the ramp up, the EV camera saw an influx of on events, and an image of the object was observable.

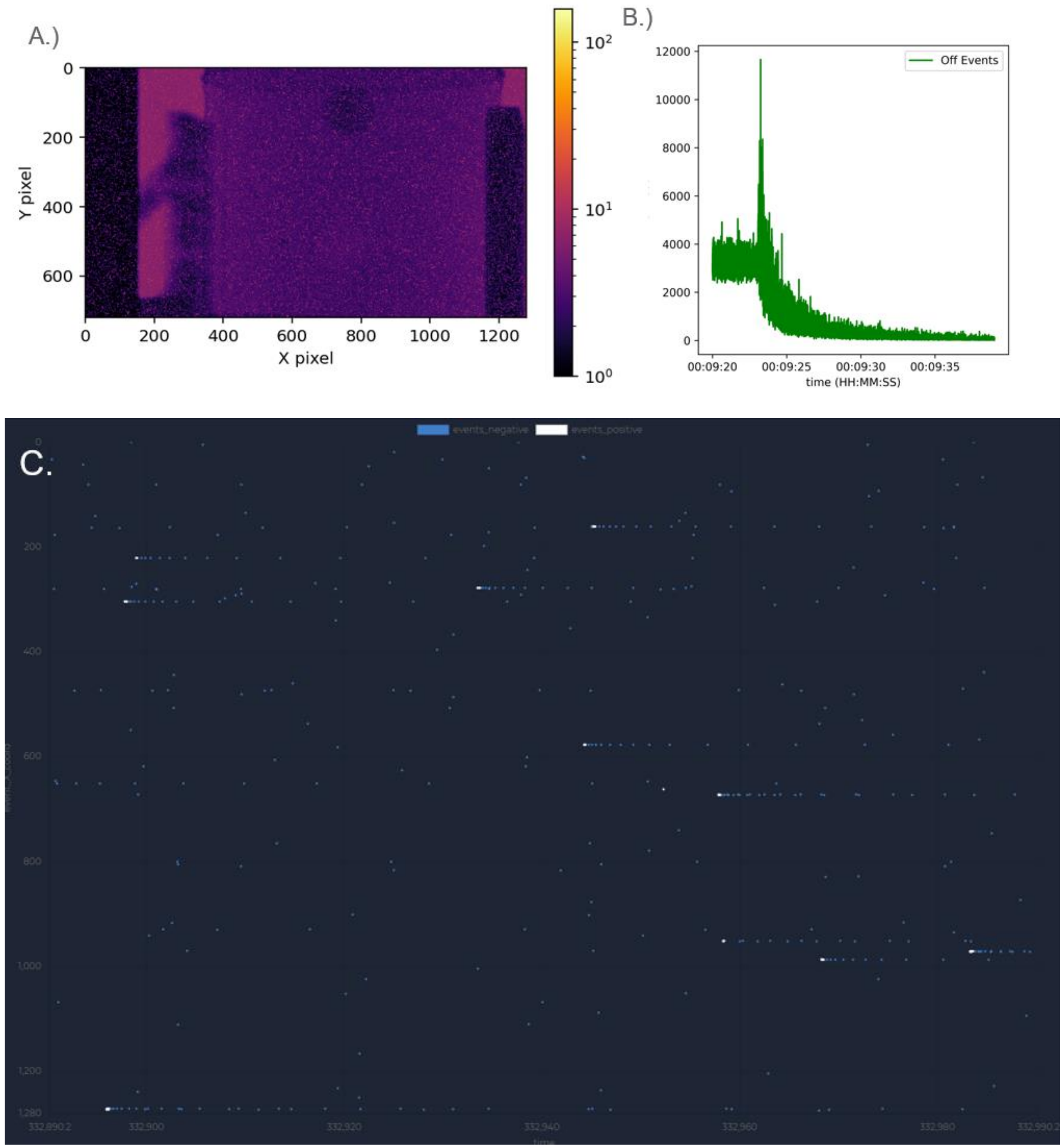


Figure 12: X-ray image when the X-ray tube turned off. During the off procedure, the EV camera saw an influx of off events, and an image of the object was observable. C.) The temporal profile of events per pixel along the x-coordinate. The profile shows an *on* event, and a stream of *off* events corresponding to the decay of Gadox.

During the measurement, there was a clear influx of events of about 5 mega events per second compared to the 5,000 events per seconds observed when the X-ray tube was off. The camera is designed to see changes in intensity, and having the EV camera in front of the X-ray system failed to show relevant contrast changes. Notably, the event camera observed scintillation. This is clear by the series of *off* events followed by a singular *on* event. When images are constructed for 1 second, some contrast is noticeable for some features in the image. However, the overall image is grainy, and the object is not clear unless an observer is aware of what the object should be.

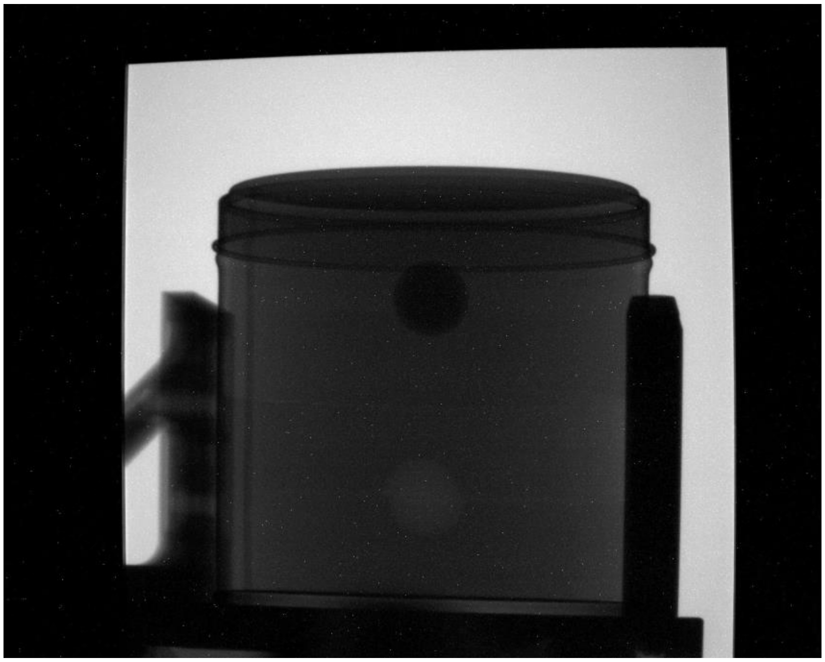

Figure 13: X-ray image of an object captured with the CMOS camera. The CMOS camera was able to capture the contrast difference of the object through most of the X-ray measurement.

## 4.2 Temporal Images

Instead of investigating the total number of events, EV cameras provide excellent timing information related to when the scintillation flash happens. A conventional camera has frame rate limitations (typically <100 fps), and two flashes that are made at not quite the same time are captured in the same frame. With an EV camera, low latency and asynchronous readout scintillation that occur a few hundred microseconds apart can be discerned. This allows immediate detection of scintillation, spatially and temporally. One way to see scintillation flashes is to convert the images to temporal format, as described in section 3.3.

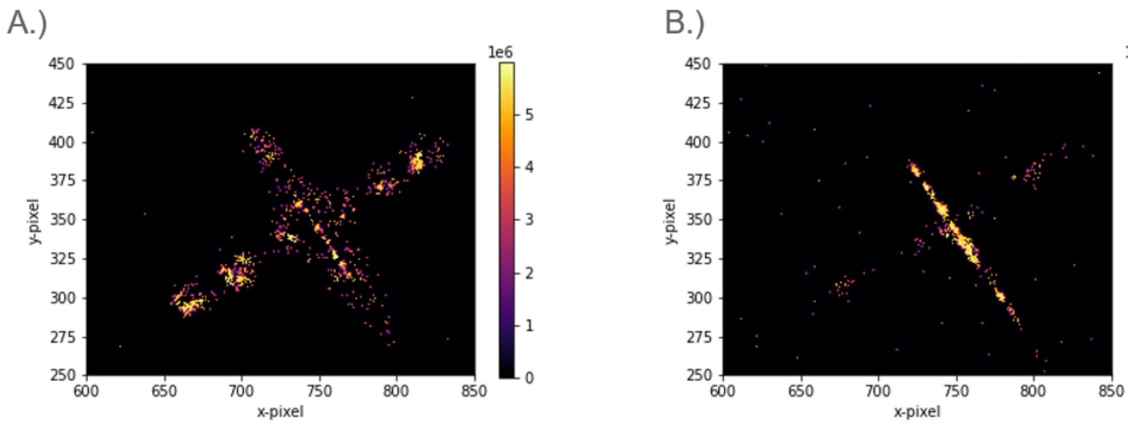


Figure 14: Time stamp of an event can be mapped to the pixel location to obtain a heat map showing the time when the event occurred. A.) Heat map of the time of on events for the scintillations. B.) Heat map of the time of off events for the scintillation.

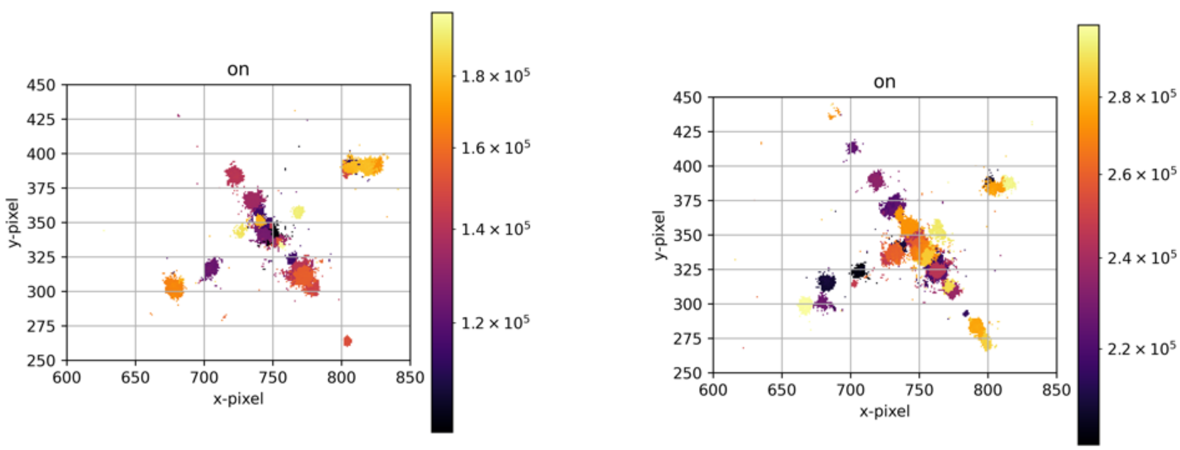


Figure 15: (Right): Imaging a Po-210 250 $\mu Ci$ source and replacing the pixel value with the time stamp of an event over a large time interval. The places where a large scintillation occurs are easily apparent. (Left): For this case, the image intensifier gain was increased. The z-axis is in units of showing when the events occurred with units of microseconds.

By converting the event data to temporal images, it is clear to see where and when scintillation flashes occur in the image. Subsequently, by applying a clustering algorithm, the clusters can be easily found in this format compared to the summed event images. In the case of summed event images, there are some cases where scintillation flashes overlap, and it is not possible to discern the difference between the two flashes (Figure 14). By contrast, in the case of temporal images, overlapping scintillation flashes are separated by time. The places with the same time color coding that occupy the same region are scintillation flashes. In many cases, the scintillation is sparse and not well-connected. This makes connected regions or clusters more difficult to find. In contrast, the time-binned images in Figure 15 show that the scintillation cluster events are visually discernible from one another.

A connected components algorithm was applied to find scintillation clusters in the temporal images for Po-210, and the count rate was found to be $19.67 \pm 1.02$ CPS. The alpha measurement had the same configuration in section 4.1.1.This is an improvement over the event count images, but it is still lower than what was measured with the iQID system. As mentioned earlier, this could be from overcounting with the iQID system. In addition, the beta source showed $35.88 \pm 1.82$ CPS when connected components were applied to find clusters. The beta measurement had the same configuration in section 4.1.2.The underestimation is likely due to the beta events being much smaller and likely being filtered out along with the noise. Attempts to lower the median filter resulted in overestimating the count rate.

# Conclusion and Path Forward

In conclusion, an EV camera was tested for measuring high-energy particles to include alpha, beta, and X-ray. To quantify the EV camera's performance, conventional measurements of the same experiment were also conducted to help ground truth the results captured with the EV camera. In addition, tests were conducted that fully leveraged the unique capabilities of the EV camera not achievable with a conventional camera system, such as dual measurements of multiple sources and measurements of high-activity sources. Finally, the event camera is can capture an X-ray image dynamically as the source strength changes.

For measuring alpha and beta sources, the event camera can provide the same qualitative features. Further work is needed to quantitatively benchmark the expected count rates of sources. Importantly, the EV camera can measure high-activity sources without saturating the detector compared to the CMOS frame-parsing iQID system. In addition, the EV camera can image both beta and alpha particles in the same image, which difficult with the lower dynamic range CMOS sensor currently used in iQID.

To make the EV camera a viable alternative to using a CMOS camera, the quantifying of clusters needs to be improved. This is likely a multilayered task and will consist of improving the overall measurement process and image processing. First, optimizing the gain on the image intensifier will likely lead to improved results. As noted in Figure 14, some of the scintillation clusters are sparse and not well connected. When the image intensifier gain is increased, this may result in a more homogenous cluster for a given scintillation flash. Unfortunately, this also increases noise. In addition, adjusting the bias setting of the EV camera will likely improve the detection of scintillation flashes and can also reduce noise. The default bias setting was used throughout this study to serve as a baseline and default. Finally, improving the processing to reduce noise and better identify clusters will further improve the results. Other clustering algorithms, such as k-means, density-based spatial clustering of applications with noise (DBSCAN), or a Gaussian mixture model, might be more suited for finding clusters for a given event stream. Ideally, a clustering approach that can find clusters in 3-D space would be more suitable for the EV camera. Connected components were used for this study due to their simplicity and to draw a fair comparison because the current system employs connected components.

For X-ray imaging, the EV camera was able to capture an image of the object. However, though events are clearly being produced, a clear image is not formed. This is likely due to the EV camera being exposed to the X-ray constantly, creating large amounts of light in the Gadox scintillator. Gadox also has a much slower decay time than the scintillators used in iQID (~2000 μs vs. 0.2 μs). The X-ray imaging CMOS detector integrates many frames to generate high contrast images instead of counting individual photon interactions (like iQID). As such, the brightness and slowness of the decay light means the EV camera was effectively seeing a static scene. This aligns with the fact that the object was temporarily observed as the source was ramping down (when the flux was lowered, and the decay of light was changing). It seems the EV camera is not suitable for static X-ray measurement but may see better performance for a moving object or when the X-ray source strength changes over time. However, further study is required to fully rule out EV cameras from being able to capture static X-ray images. Using lower x-ray current and/or a faster scintillator may result in improved performance for the EV camera for X-ray imaging.

# 5.0 References


1. Gallego, G., et al., Event-based vision: A survey. IEEE transactions on pattern analysis and machine intelligence, 2020. 44(1): p. 154-180.

2. Rebecq, H., et al., High speed and high dynamic range video with an event camera. IEEE transactions on pattern analysis and machine intelligence, 2019. 43(6): p. 1964-1980.

3. Li, B., et al., Enhancing 3-D LiDAR point clouds with event-based camera. IEEE Transactions on Instrumentation and Measurement, 2021. 70: p. 1-12.

4. Zhou, Y., G. Gallego, and S. Shen, Event-based stereo visual odometry. IEEE Transactions on Robotics, 2021. 37(5): p. 1433-1450.

5. Mitrokhin, A., et al. Event-based moving object detection and tracking. in 2018 IEEE/RSJ International Conference on Intelligent Robots and Systems (IROS). 2018. IEEE.

6. Zhang, A., et al., Event-based x-ray imager with ghosting-free scintillator film. Optica, 2024. 11(5): p. 606-611.

7. Sleator, C., et al. X-ray tracking using a perovskite scintillator with an event-based sensor. in Hard X-Ray, Gamma-Ray, and Neutron Detector Physics XXV. 2023. SPIE.

8. Clarke, A.M., et al., Characterization of a large-area iQID imager for safeguards applications. Nuclear Instruments and Methods in Physics Research Section A: Accelerators, Spectrometers, Detectors and Associated Equipment, 2020. 954: p. 161125.

# Pacific Northwest National Laboratory

902 Battelle Boulevard
P.O. Box 999
Richland, WA 99354

1-888-375-PNNL (7665)

***www.pnnl.gov***